Biosensors and Bioelectronics 145 (2019) 111728

Contents lists available at ScienceDirect

Biosensors and Bioelectronics

journal homepage: http://www.elsevier.com/locate/bios

Label-free and highly selective electrochemical aptasensor for detection of PCBs based on nickel hexacyanoferrate nanoparticles/reduced graphene oxides hybrids

Lifang Fan[a,*], Guizhen Wang[a], Wenting Liang[a], Wenjun Yan[b], Yujing Guo[a,**], Shaomin Shuang[a], Chuan Dong[a,***], Yingpu Bi[c]

[a] Institute of Environmental Science, College of Chemistry and Chemical Engineering, Shanxi University, Taiyuan, Shanxi, 030006, PR China
[b] Analytical Instrumentation Center, Institute of Coal Chemistry, CAS, Taiyuan, 030001, PR China
[c] State Key Laboratory for Oxo Synthesis & Selective Oxidation, Lanzhou Institute of Chemical Physics, CAS, Lanzhou, 730000, PR China

ARTICLE INFO

Keywords:
Aptasensor
Reduced graphene oxides
PCB77
Nickel hexacyanoferrate

ABSTRACT

In consideration of the urgent need to determine polychlorinated biphenyls (PCBs) in the environment, a label-free and highly selective electrochemical aptasensor was constructed for determining PCBs based on nickel hexacyanoferrate nanoparticles (NiHCF NPs)/reduced graphene oxides (rGO) hybrids. NiHCF NPs/rGO hybrids with small size of about 5 nm NiHCF NPs were synthesized for the first time by in situ co-deposition of NiHCF NPs on rGO surface. In the hybrids, rGO with large area and good conductivity can supply more space for loading NiHCF NPs and improve the conductivity of the hybrids. NiHCF NPs that can be used to be act as a signal probe exhibit a couple of well-defined peaks with highly reversible redox ability and good stability. Here, PCB77 as a model molecule, the anti-PCB77 aptamer was anchored on the NiHCF NPs/rGO hybrids by covalent bonding reaction. The design aptasensor for detecting PCB77 exhibits a favorable linear response from 1.0 to 100.0 ng/L with a low detection limit of 0.22 ng/L. Meanwhile, it displays good selectivity for PCB77 detection due to the specificity and high affinity of aptamer to PCB77. Additionally, the application of the aptasensor was evaluated in real environmental samples.

1. Introduction

Polychlorinated biphenyls (PCBs) are a kind of common persistent environmental pollutants, which are comprising 209 congeners. PCBs have been widely applied in different industries due to their highly chemical stability, thermal stability, and low conductivity (Kezios et al., 2012; Habibullah-Al-Mamun et al., 2019). Since the highly toxic effect of PCBs on human which can cause thyroid dysfunction, endocrine disorder and carcinogenicity have been identified, commercial production and usage of PCBs has been banned in the 1970s. However, whether accidental or deliberate, the release of PCBs is inevitable because of their long service life in the environment, and they are still frequently found in the global environment, animal-source food and natural waters (Murati et al., 2017; Zhu et al., 2012). Therefore, it is significant for monitoring PCBs in the environment for protection environmental and human health.

PCB analysis is mainly performed using gas chromatography (GC) and high-performance liquid chromatography (HPLC), coupled with mass spectroscopy (MS) (Peng et al., 2015; Chamkasem et al., 2016). Although these instrumental analyses are sensitive and accurate, they always require complicated instruments and trained operators, and the sample pretreatment is time-consuming and tedious. By contrast, electrochemical techniques have attracted wide attention owing to these merits including simple operation, favorable portability, fast response and high sensitivity (Sun et al., 2019). However, PCBs are a kind of electrochemically inert molecules, which are difficult to be determined directly by electrochemical oxidation. So some molecularly imprinted polymer (MIPs)-based sensors (Kubo et al., 2007; Mkhize et al., 2017) and electrochemical immunosensors (Verdian et al., 2019; Greathead et al., 2016) have been developed for detection of PCBs. The techniques

---

* Corresponding author.
** Corresponding author.
*** Corresponding author.
E-mail address: flf@sxu.edu.cn (L. Fan).

https://doi.org/10.1016/j.bios.2019.111728
Received 19 June 2019; Received in revised form 18 September 2019; Accepted 20 September 2019

exhibit high sensitivity and good selectivity, meanwhile, which can simplify complicated analysis procedures and shorten the detection time compared with those conventional instrumental analyses. But their disadvantages can't also be ignored because the MIPs-based electrochemical sensors are often suffered from weak force, slow recognition process and incomplete removal of imprinting molecules. Similarly, the electrochemical immonsensors based on antibodies are susceptible to environmental conditions, and antibodies extraction procedures are complicated and time-consuming. Aptamers, single stranded DNA or RNA ligands that exhibit high specificity to their targets (Tuerk and Gold, 1990; Sassanfar and Szostak, 1993) become an appropriate alternative to MIPs or antibodies. At present, aptamer-based sensors have attracted more and more interesting for selective detection of analytes. Now, there have been the related reports about some aptamers selected for high affinity and specific binding to PCBs (Mehta et al., 2012; Yan et al., 2015; Lu et al., 2014; Yang et al., 2018). Therefore, we propose to develop an electrochemical aptasensor by combining the specificity of aptamer to individual PCBs with high sensitivity of electrochemical method for efficiently detection of PCBs in the environment.

A crucial point is noted that how to transduce the binding events between aptmer and its target into a detectable signal during designing of electrochemical aptasensors. In general, electroactive substances including methylene blue (Xu et al., 2019; Zhad et al., 2017), ferrocene (Magriñá et al., 2019; Chen et al., 2019) and ruthenium compounds (Vidimara et al., 2019) have been explored to label aptamer or added directly to test system to obtain a detectable signal. However, the entire procedure of labeling aptamer is complex and time-consuming, and could destroy the affinity of aptamer. The addition of electroactive substances in test system could generate false-positive results arising from electrode contamination or excessive testing. Thus, it is a good idea for the introduction of an in situ signal probe on the electrode to overcome the above shortcomings.

Transition metal hexacyanoferrates, a class of zeolite-like Prussian blue coordination compounds have been extensively studied due to their unique properties such as electrocatalytic activity (Narendra Kumar et al., 2018), supercapacitance (Ma et al., 2017), ion-sensing (Bagkar et al., 2006) and ion-exchange (Ciabocco et al., 2013). Among transition metal hexacyanoferrates, nickel hexacyanoferrate (NiHCF) displays well-defined, reversible and reproducible responses in the solution containing alkali-metal cations, which is qualified for acting as an electron transfer mediator for development of label-free aptasensors.

Herein, small size of 5 nm NiHCF nanoparticles (NiHCF NPs) deposited on reduced graphene oxide (rGO) have been synthesized by an in situ co-precipitation method. The introduction of rGO not only improve the conductivity of the hybrids and promote the electron transfer, but provide a mass of active sites for deposition of NiHCF NPs. Through the combination of NiHCF NPs with rGO, NiHCF NPs/rGO hybrids possesses excellent electrochemical properties. PCB77 as a model molecule, the NiHCF/rGO hybrids have been coated on gold electrode surface for the immobilization of amino-terminal aptamer molecules by covalent reaction between –NH_2 and –COOH groups on the hybrids. Thus, a label-free and highly selective electrochemical aptasensor has been developed based on NiHCF/rGO hybrids for determination of PCB77. With the addition of PCB 77, PCB77-aptamer complexes formed on sensing surface increase the resistance of the electron transfer on the electrode, resulting in the decrease of the current. The current change is used to determine PCB77 quantitatively. The analytical behavior of the electrochemical aptasensor has been investigated in detail. Additionally, the aptasensor has been applied in detection of PCB77 in the environmental samples.

2. Experiment

2.1. Reagents and apparatus

The oligonucleotide sequence was synthesized from Sangon Biotechnology Co. Ltd. (Shanghai, China).

5′-GGC-GGG-GCT-ACG-AAG-TAG-TGA-TTT-TTT-CCG-ATG-GCC-CGT-G-$(CH_2)_6$ –NH_2-3'.

PCB77 and PCB81 were purchased from Beijing Lark Company (Beijing, China). Poly (diallyldimethylammonium chloride) (PDDA) (20%, Mw ca.65,000), N-hydroxy succinimide (NHS) and1-Ethyl-3-(3-dimethylaminopropyl) carbodiimide (EDC) were purchased from purchased from Aladdin Reagent Co., Ltd. All of the apparatuses are supplied in supporting material.

2.2. Preparation of rGO and NiHCF NPs/rGO hybrids

According to the prior literature (Wu et al., 2017), the preparation of rGO was given in supporting material. The NiHCF NPs/rGO hybrids were fabricated by in situ co-precipitation of NiHCF NPs on rGO surface. First, 10.0 mM $K_3[Fe(CN)_6]$ was slowly added to 10.0 ml rGO solution (0.25 mg/mL) under stirring vigorously to prevent rGO agglomeration. The $Fe[(CN)_6]^{3-}$ would be adsorbed on rGO sheets because of electrostatic interaction. Then, the pH value of the solution was adjusted to 3.0 using 0.1 M HCl, and the same volume of $Ni(NO_3)_2$ (10.0 mM) with $K_3[Fe(CN)_6]$ was injected into the mixture and stirred for 4 h. Finally, the NiHCF NPs/rGO hybrids were prepared through centrifugation and rinsed by using deionized water. For comparison, NiHCF NPs/rGO hybrids with different size NiHCF NPs were pepared. The pure NiHCF NPs were prepared using the similar strategy with that of NiHCF NPs/rGO hybrids without rGO.

2.3. Preparation of electrochemical aptasensor

The gold electrode (2 mm in diameter) was polished with 1.0, 0.3 and 0.05 μm alumina slurry, respectively. Subsequently, the polished electrode was sonicated in absolute ethanol and deionized water for 30 s, respectively. Then, it was put in 0.5 M H_2SO_4 by scanning from 0.0 V to 1.6 V until a steady-state cyclic voltammogram was present. 3.0 μL NiHCF NPs/rGO hybrids was dropped on the as-prepared electrode surface and then dried in N_2 atmosphere. The NiHCF NPs/rGO hybrids modified electrode was incubated in 2.0 μM aptamer solution containing 20 mg/mL EDC and 10 mg/mL NHS overnight at 4 °C. Thus, amino-terminal aptamer was anchored on NiHCF NPs/rGO hybrids by the covalent reaction between –NH_2 and –COOH groups on the hybrids. Finally, the aptamer-modified electrode was incubated in 10.0 μL, 2.0 wt % BSA at room temperature for 1 h to block any possible remaining active sites and reduced non-specific adsorption. The electrochemical aptasensor based on NiHCF NPs/rGO hybrids was prepared and stored at 4 °C. The preparation process of the electrochemical aptasensor and the mechanism for PCB77 detection are shown in Scheme 1.

2.4. Electrochemical experiments

All electrochemical experiments were performed in 0.1 M PBS solution (pH 7.41) by cycle voltammetry (CV) or differential pulse voltammetry (DPV). The electrochemical impedance spectroscopy (EIS) measurements were performed in 5.0 mM $K_3[Fe(CN)_6]/K_4$ $[Fe(CN)_6]$ containing 0.1 M KCl, and recorded between 0.1 Hz and 1000 Hz with a sinusoidal voltage perturbation of 10 mV amplitude. Chronocoulumetry measurements were carried out in 0.1 mM $K_3[Fe(CN)_6]$, and 0.1 M PBS (pH 7.41) containing 1.0 mM $[Ru(NH_3)_6]Cl_3$.

3. Results and discussion

3.1. Materials characterization

GO was first reduced to rGO by hydration hydrate. The characterization results of the UV–vis and IR of GO and rGO in supporting material (Fig. S1) show that GO has been successfully reduced to rGO. Afterwards, NiHCF NPs/rGO hybrids were prepared by co-precipitation

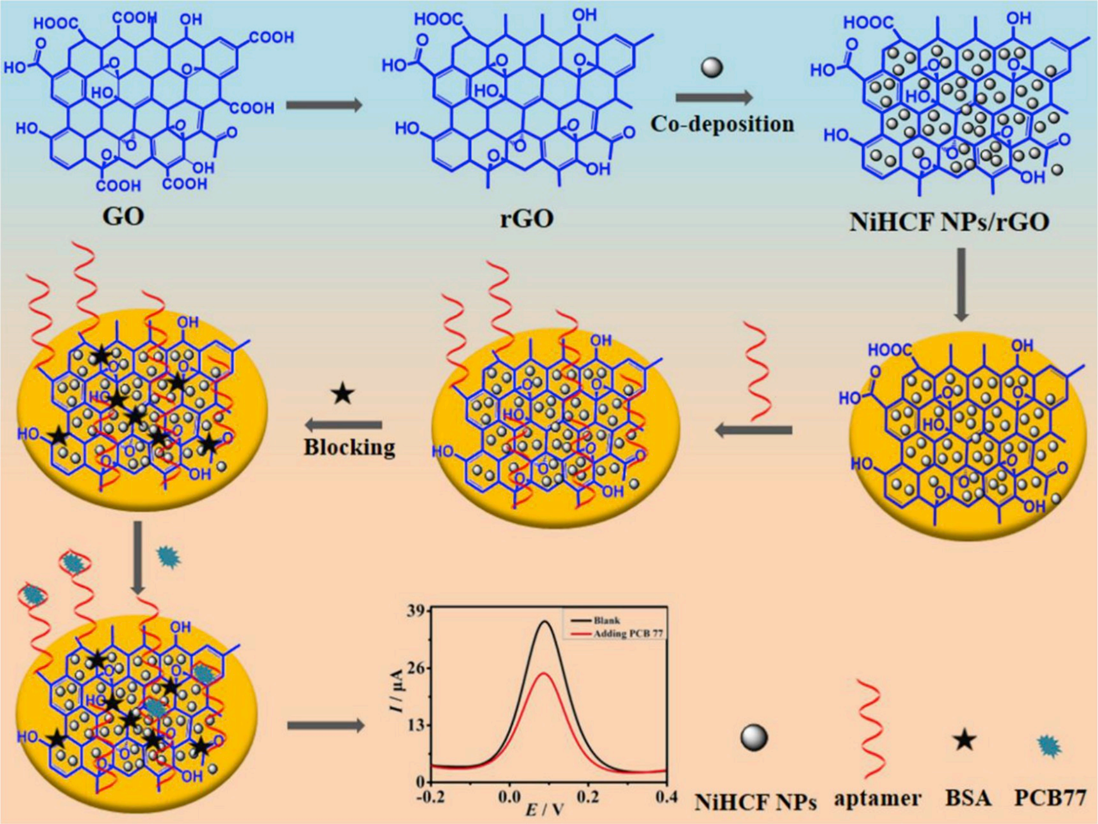

Scheme 1. Schematic representation of the electrochemical aptasensor construction and the mechanism for detection of PCB77.

of $Ni(NO_3)_2$ and $K_3[Fe(CN)_6]$ on rGO. TEM images of NiHCF NPs/rGO hybrids under different magnification are illustrated in Fig. 1A–C (TEM image of rGO in Fig. S2). For the NiHCF NPs/rGO hybrids in Fig. 1A and B, NiHCF NPs with the average size of about 5 nm are uniformly dispersed on rGO and show obvious lattice fringes under high resolution TEM (Fig. 1C). Also, there are hardly any NiHCF NPs outside the rGO sheets, demonstrating that the strong interaction between NiHCF NPs and rGO. The composition of NiHCF NPs/rGO hybrids was determined via EDS. Fig. 1D displays that Ni, Fe, C, O and N elements are present in NiHCF NPs/rGO hybrids. The elemental mapping confirms that the five elements are highly dispersed on NiHCF NPs/rGO hybrids. Furthermore, the EDS analysis shows that the atom percent of Ni and Fe is 3.11% and 2.94% (Table S 1), and the atom ratio of Ni and Fe is 1:1, corresponding the stoichiometry of Ni $[Fe(CN)_6]^-$ present in the NiHCF NPs. The crystal structure of NiHCF NPs/rGO hybrids and pure NiHCF NPs were measured by XRD technique. Fig. 1E shows all the diffraction peaks of the pure NiHCF NPs (curve a) can be indexed as cubic NiHCF (JCPDS no. 51–1897) (Chen et al., 2009). The XRD pattern of NiHCF NPs/rGO hybrids (curve b) is the same with the pure NiHCF NPs except an inconspicuous broad peak associated with C (002) plane from the rGO present at the diffraction angle of 15–30° (Kottegoda et al., 2011). Furthermore, the peak intensity of NiHCF NPs/rGO hybrids become lower than that of NiHCF NPs, which may be relate to the crystallized originating from the small particle size of NiHCF NPs. This result is consistent with that of the previous TEM. The Raman spectra of NiHCF NPs/rGO hybrids and pure NiHCF NPs are shown in Fig. 1F. A single resolvable high wave number peak at 2186 cm^{-1} for the pure NiHCF NPs (curve a) is assigned to the stretching vibration of the CN region of cyanide coordinated to Fe(III) (Jeerage et al., 2002). For the NiHCF NPs/rGO hybrids (curve b), there are two prominent peaks at 1348 cm^{-1} and 1600 cm^{-1}, assigning to D and G bands. Also, I_D/I_G value for NiHCF NPs/rGO hybrids is 1.06, which is lower than that of GO (Zhou et al., 2019). These results demonstrates the combination of NiHCF NPs with rGO lowers graphitization degree and provides rapid electron pathway, leading to better electrochemical properties of NiHCF NPs/rGO hybrids compared to that of the pure NiHCF NPs. Besides, the composition of NiHCF NPs/rGO hybrids was further investigated by XPS. Fig. 2A illustrates the survey spectrum of NiHCFNPs/rGO hybrids, the binding energies of C 1s, N 1s, O 1s, Ni 2p and Fe 2p can be clearly observed. Meanwhile, the high-resolution spectra of the five elements are shown in Fig. 2B–F. Seen from the high-resolution spectra of Fe (Fig. 2B), Fe $2p_{3/2}$ and $2p_{1/2}$ at 709.4 and 722.3 eV is assigned to +3 oxidation state produced in hybrids, which is well agree with that of the Raman characterization. In XPS spectrum of Ni (Fig. 3C), Ni $2p_{3/}$and $2p_{1/2}$ peaks appear at 862.4 and 881.5 eV, indicating that oxidation state is mainly Ni^{2+} (Jiang et al., 2015). The peak at 402.5 eV in the high-resolution spectra of N1s in Fig. 3D is assigned to the quaternary ammonium group formed by PDDA-stabilized rGO (Liu et al., 2013). And another N1s signal for cyano group appears at 397.7eV (Li et al., 2012a), further confirming that NiHCF NPs have been deposited on rGO sheets. The C1s fitted spectra curves in Fig. 2E display that the peak at 284.8 eV is arising from C–C, and other three peaks at 286.6, 288.0 and 289.0 eV are ascribed to hydroxyl, carbonyl and carboxylate. Compared with pure GO in the previous reported work (Fan et al., 2019), the peak at 284.8 eV become dominant while the three peaks of oxygen-containing groups are weaken, further confirming that GO has been reduce to rGO. The O1s high-resolution spectrum in Fig. 2F displays this peak is assigned to epoxide group. These results are consistent with the previous reports (Yang et al., 2015; Youn et al., 2015). In addition, the electrochemical properties of rGO, pure NiHCF NPs and NiHCFNPs/rGO hybrids were investigated by CV. As shown in Fig. 3A, there is no redox peak present for the rGO (curve a). For the pure NiHCF NPs (curve b), a pair of redox peaks occurs at the midpoint potential of 0.35 V, ascribing to electron shift between Fe^{2+} and Fe^{3+} ions accompanied by Na^+ uptake/release in the unit cell of NiHCF NPs, (Li et al., 2012b). Similarly, a couple of redox peaks is observed on NiHCF NPs/rGO hybrids modified electrode (curve

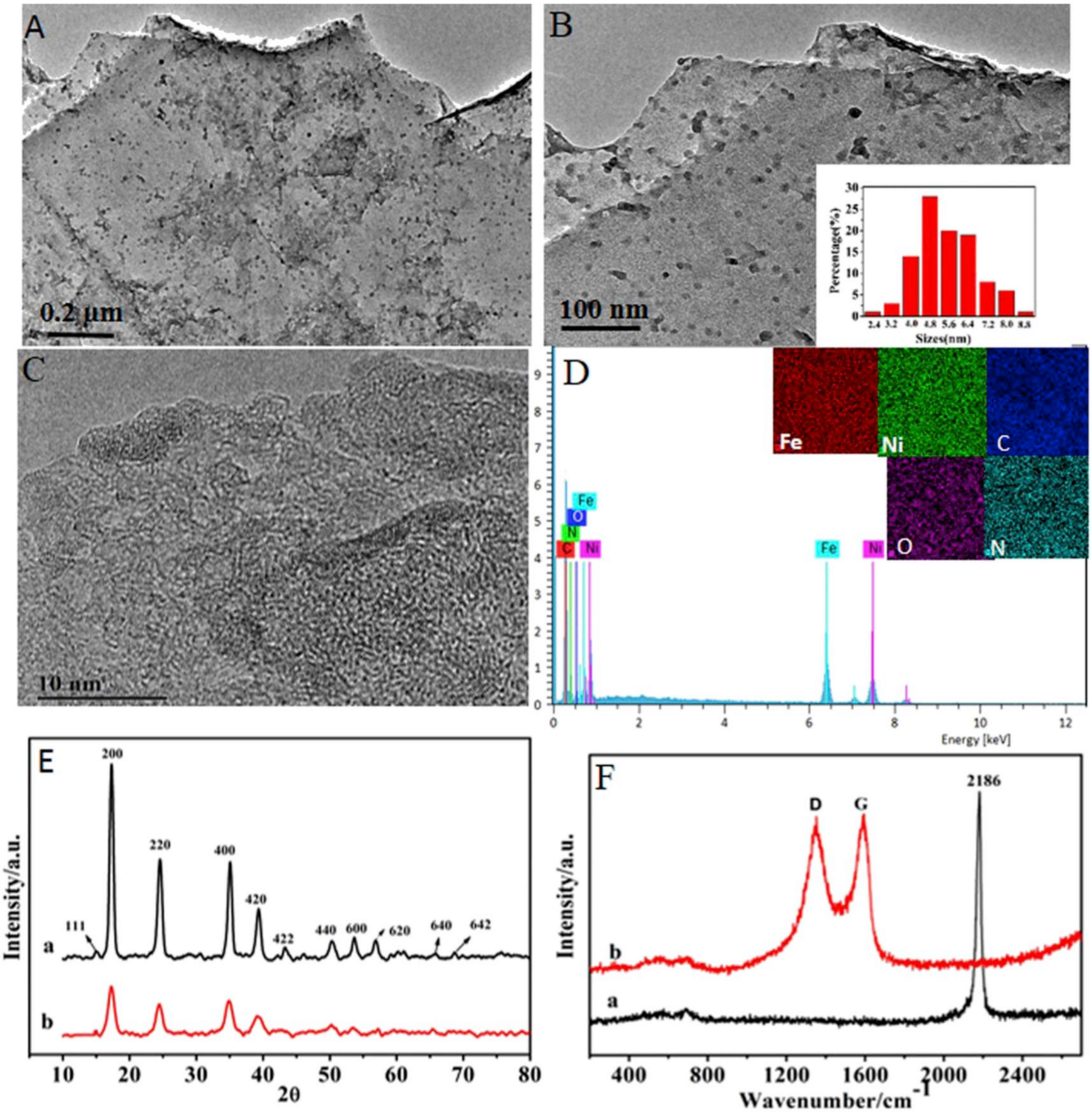

Fig. 1. TEM images of NiHCF NPs/rGO hybrids under different magnificent (A–C), Inset: the histogram of size distributions for NiHCF NPs on rGO; EDS curve (D) of the NiHCF NPs/rGO hybrids, Inset: the elemental mapping of Fe (red), Ni (green), C (blue), O (purple) and N (blue green) with color superposition in NiHCF NPs/rGO hybrids; XRD patterns (E) and Raman spectrum (F) of pure NiHCF NPs (a), and NiHCF NPs/rGO hybrids (b). (For interpretation of the references to color in this figure legend, the reader is referred to the Web version of this article.)

c). The redox peaks of NiHCF NPs/rGO hybrids exhibit a smaller the peak separation ΔE_p, and the ratio of the anodic and cathodic current (I_{pa}: I_{pc}) is close to one, compared with the pure NiHCF NPs, demonstrating that this electrochemical process of NiHCF NPs/rGO hybrids is more reversible and faster than that of the pure NiHCF NPs. Moreover, the peak current of NiHCF NPs/rGO hybrids is more than twice that of the pure NiHCF NPs. Also, EIS measures were performed to investigate their electrochemical properties, shown in Fig. 3B. The EIS spectra can be modeled with equivalent circuit models (Inset of Fig. 3B), which has been proved to be a powerful tool for interpreting the electrical properties of the electrode interface. In the circuit, R_{et} is the charge-transfer resistance which reflects blocking behavior of the electrode interface, C is the differential capacitance, Z_w is Warburg impedance, and R_s is the solution-phase resistance. Fig. 3B displays the EIS value of 2496.2 Ω for the rGO modified electrode (curve a), while the EIS value (curve b) increases greatly to 9106.4 Ω for NiHCF NPs, implying that NiHCF NPs with poor conductivity inhibit the electron transfer between the electrode and the solution. Amazingly, the EIS value obviously decreases to 5498.3 Ω for NiHCF NPs/rGO hybrids modified electrode (curve c), which is ascribed to the fact that combination of NiHCF NPs and rGO dramatically improves the conductivity of NiHCF NPs. Beside, DPV responses of these materials were also investigated, and the detailed characterization results shown in Fig. S3 were consistent with that of CV and EIS characterization. These results demonstrate that NiHCF NPs/rGO hybrids exhibit the excellent electrochemical behavior, which may be ascribed to the combination of the small size of NiHCF NPs and the synergic effect from rGO.

When NiHCFNPs/rGO hybrids were coated on the gold electrode, the surface coverage, Γ was calculated according to the equation (Laviron, 1979), $\Gamma = Q/nFA$. Γ is 3.110×10^{-9} mol cm^{-2}, and the calculation process has been supplied in Figs. S4–S5. Meanwhile, the electrochemical performance of the NiHCF/rGO hybrids modified electrode was studied at different scan rates, shown in Fig. 3C. The redox peak current of NiHCF NPs/rGO electrode is linearly proportional to different scan rates (Inset of Fig. 4A), implying that the electrochemical process is a diffusionless system. Besides, the stability of NiHCF NPs/rGO electrode was studied by CV. As illustrates in Fig. 3D, the current of NiHCF NPs/rGO modified electrode has hardly change, and the peak separation remains constant through successive scanning for 25 cycles, demonstrating these electroactive sits of NiHCF NPs/rGO hybrids have no any

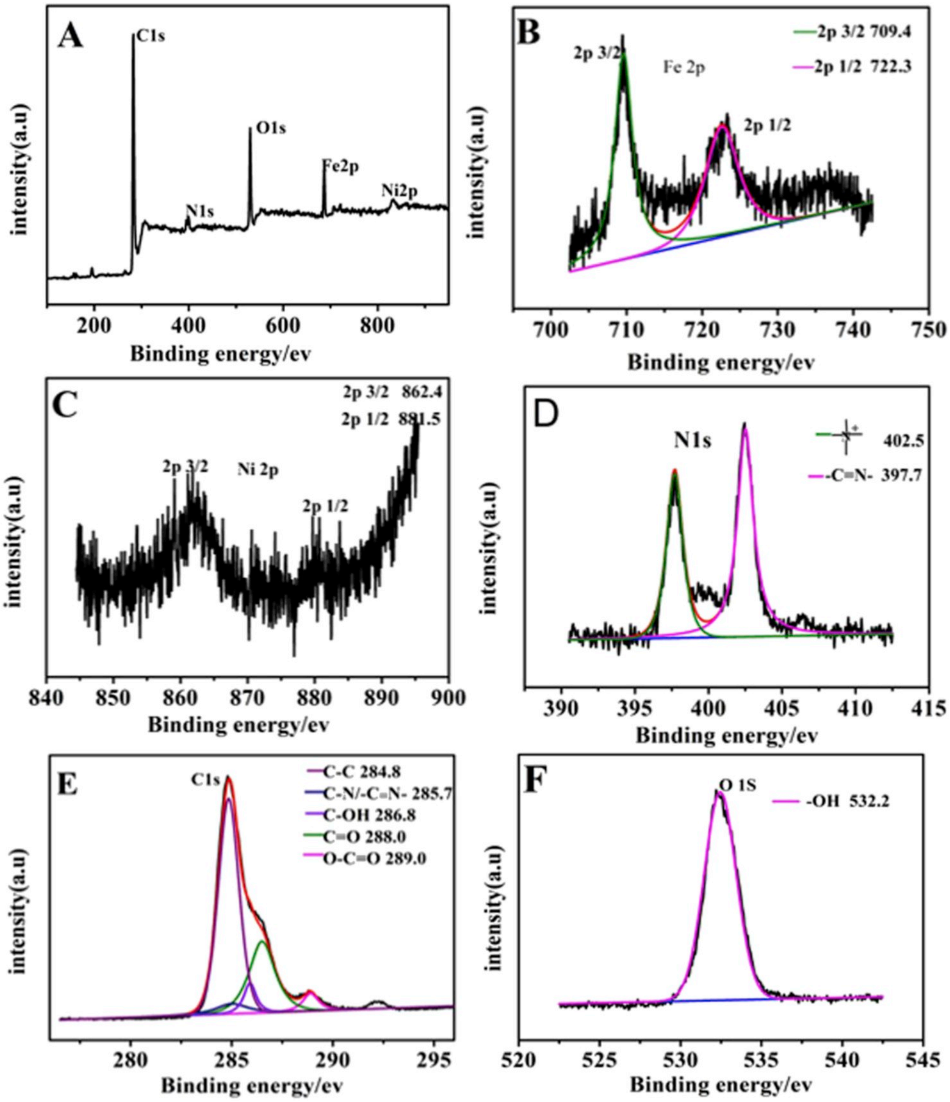

Fig. 2. XPS survey profiles of NiHCF NPs/rGO hybrids (A); The high-resolution spectra of (B) Fe 2p, (C) Ni 2p, (D) N1s, (E) C1s and (F) O1s in NiHCF NPs/rGO hybrids.

loss after the long term storage in air and possess good stability.

3.2. Fabrication of electrochemical aptasensor

The construction steps of the aptasensor were studied by CV. As shown in Fig. 3E, no any peak is observed on the bare electrode (curve a). Only rGO is dispersed on the electrode, there is still no peak present (curve b). While depositing NiHCF NPs/rGO hybrids, a pair of redox peaks (curve c) is present, which can be arising from the redox couple of Fe^{3+}/Fe^{2+}, demonstrating the hybrids have been firmly immobilized on the electrode. When aptamer molecules have been anchored on the NiHCF NPs/rGO hybrids modified electrode, the peak current decrease, and the redox peaks display poor reversibility (curve d). This is ascribed to the fact that modified aptamer molecules acted as an insulating layer hind the electron transfer between the signal indicator and the electrolyte. Finally, when the aptasensor has been used to detect PCB77, the results reveal that the current further decrease (curve e). This can be explained that the PCB77-aptamer complexes with poor conductivity further increase the hindrance of the electron transfer on sensing interface.

EIS measures were performed to characterize the preparation stages of the electrochemical aptasensor, shown in Fig. 3F. The impedance spectrum of the bare electrode exhibits a small semicircle domain with the EIS value of 178.4 Ω (curve a). Only rGO nanosheet was dispensed on the bare electrode, the EIS value increased to 2499.7 Ω (curve b). However, when NiHCF NPs/rGO hybrids were coated on the gold electrode, the EIS value increased dramatically to 5498.3 Ω (curve c). This is attributed to that the NiHCF NPs with poor conductivity hinder the electron transfer between $[Fe(CN)_6]^{4-/3-}$ and the electrode. While anti-PCB77 aptamer molecules were immobilized on the NiHCF NPs/rGO hybrids modified electrode, the corresponding diameter of semicircle further increased to 8800.2 Ω (curve d). The reason is that the negative charges of phosphate backbone in aptamer molecules make strong electrostatic repulsive force to the negatively charged probe anions $[Fe(CN)_6]^{4-/3-}$, leading to the increase of the EIS value. When the electrochemical aptasensor was utilized to detect PCB77, the diameter of semicircle remarkably increased to approximately 10,499.5 Ω (curve e), because the PCB77-aptamer complexes formed with poor conductivity inhibited electron transfer between the signal probe and the electrolyte. Besides, DPV measurements were also carried out to monitor each immobilization step of the aptasensor, the detailed results were given in Fig. S6. The results of EIS and DPV absolutely correspond with those of CV. Additionally, the surface morphology of NiHCF NPs/rGO hybrids, aptamer/NiHCF NPs/rGO and BSA/aptamer/NiHCF NPs/rGO modified

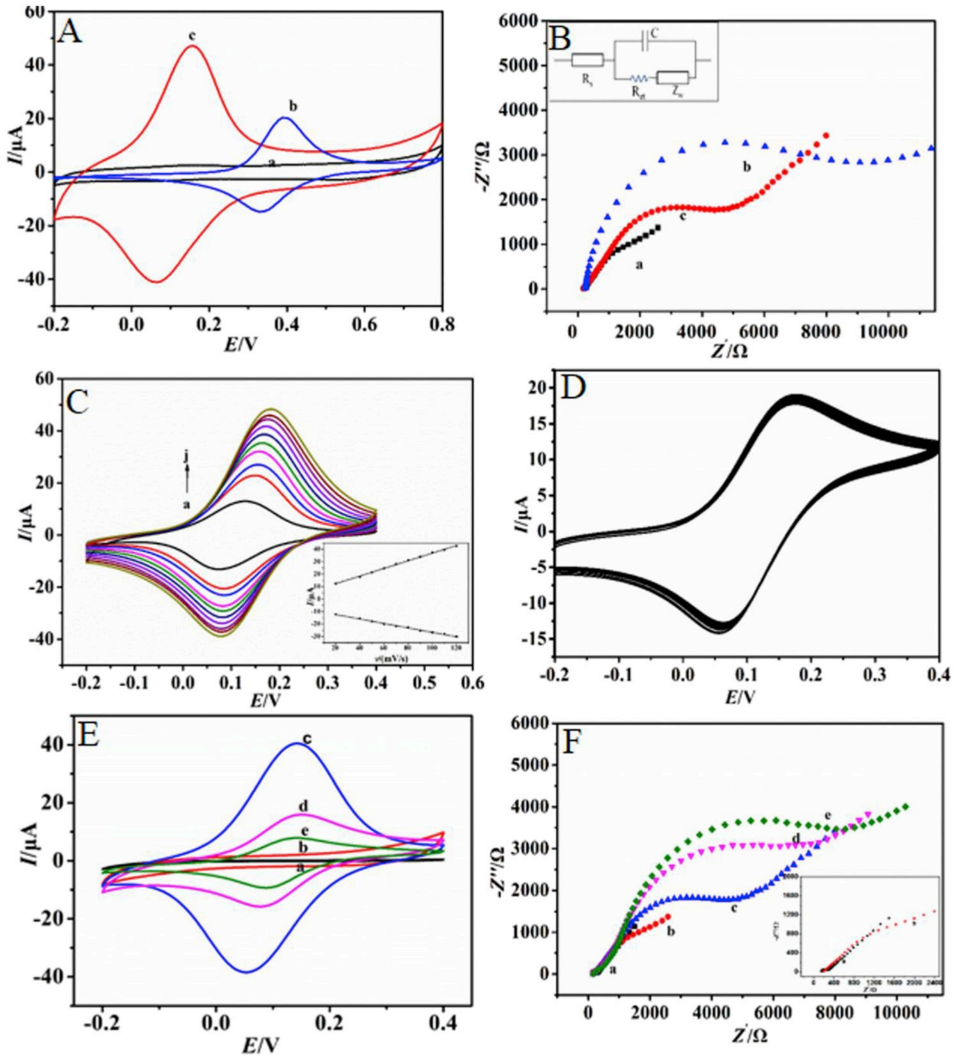

Fig. 3. (A) CV and (B) EIS curves of rGO (a) pure NiHCF NPs (b), and NiHCF NPs/rGO hybrids (c) modified electrode; (C) CV curves of NiHCF NPs/rGO hybrids modified electrode at different scan rates (from a to j: 20, 40, 50, 70, 80, 90, 100, 110, 120 mV/s); Inset: Dependence of the redox peak current on the scan rates; (D) Stability of NiHCF NPs/rGO hybrids modified electrode; (E) CV and (F) EIS curves of bare gold electrode (a), rGO (b), NiHCF NPs/rGO hybrids (c), aptamer/NiHCF NPs/rGO (d) and PCB77 being bound on BSA/aptamer/NiHCF NPs/rGO (e) modified electrode. (For interpretation of the references to color in this figure legend, the reader is referred to the Web version of this article.)

electrode were analyzed by AFM. As shown in Fig. 4A, the NiHCF NPs are dispersed uniformly on rGO, and the height of NiHCF NPs/rGO hybrids was 19.81 nm. The surface roughness (RMS) was calculated for the NiHCF/rGO hybrids with the value of 3.00 nm. It is observed clearly from Fig. 4B that the distribution of NiHCF NPs becomes sparsely because parts of NiHCF NPs have been covered. The height of 24.58 nm and the RMS value of 3.78 nm are larger than that of the pure NiHCF NPs/rGO hybrids. Also, the 3D image of aptamer/NiHCF NPs/rGO modified electrode shows a bumpy structure with a large number of ups and downs, demonstrating that the aptamer molecules have been successfully immobilized on the NiHCF NPs/rGO hybrids. After the coating of BSA as the blocker, the number of the NiHCF NPs exposure becomes more less, and the height and surface roughness further increased to 24.91 nm and 3.92 nm (Fig. 4C). The characterization results of AFM are totally consistent with that of the electrochemical measurements, indicating that the aptasensor has been successfully prepared.

3.3. Performance of electrochemical aptasensor

The electrochemical aptasensor was used to determine PCB77 with different concentrations. The DPV responses are presented in Fig. 4D. The peak current decreases with increasing the concentrations of PCB77 in the range of 1.0–100.0 ng/L. This illustrates that a mass of PCB77 have been captured by the apatamer molecules on the modified electrode, and vast PCB77-aptamer complexes formed inhibit the electron transfer between the signal probe and the electrolyte, resulting in the decrease of the peak current. When the concentrations of PCB77 are over 100.0 ng/L, the peak current keep almost unchanged, indicating the aptamer molecules on the sensing interface have absolutely interacted with PCB77. The relationship curve between the current change, ΔI and PCB77concentrations is illustrated in Fig. 4E. ΔI exhibits a good linear relationship with the logarithm of PCB77 concentrations from 1.0 to 100.0 ng/L (Inset of Fig. 4E). The regression equation is $\Delta I = 16.93$ lgC +18.11(unit of C, ng/L) with a correction coefficient of 0.9952. The limit of detection for PCB77 is 0.22 ng/L at the signal-to-noise ratio of 3. Compared the analytical behavior of the present aptasensor with the previous reported methods, the comparison results are shown in Table 1. As can be seen, the present aptasensor exhibits higher sensitivity for detection of PCB77 than that of HPLC and other optical sensors or most of electrochemical biosensors, as well as the linear range and the stability are also comparable. Although the electrochemical biosensor exhibits obviously lower detection limit of 0.033 ng/L, it requires tedious labeling aptamer and the stability of the biosensor was relatively weak. In this work, the entire procedure of detection took less than 2 h, which was time-saving compared with other methods, other than the PCB77 detection in a few of minutes with SERS sensor. Furthermore, the present aptasensor is simpler, rapider and more low-cost without expensive instruments and materials. Most importantly, the electrochemical biosensor prepared by introducing an in situ signal probe on the electrode surface successfully overcome the shortcomings caused by

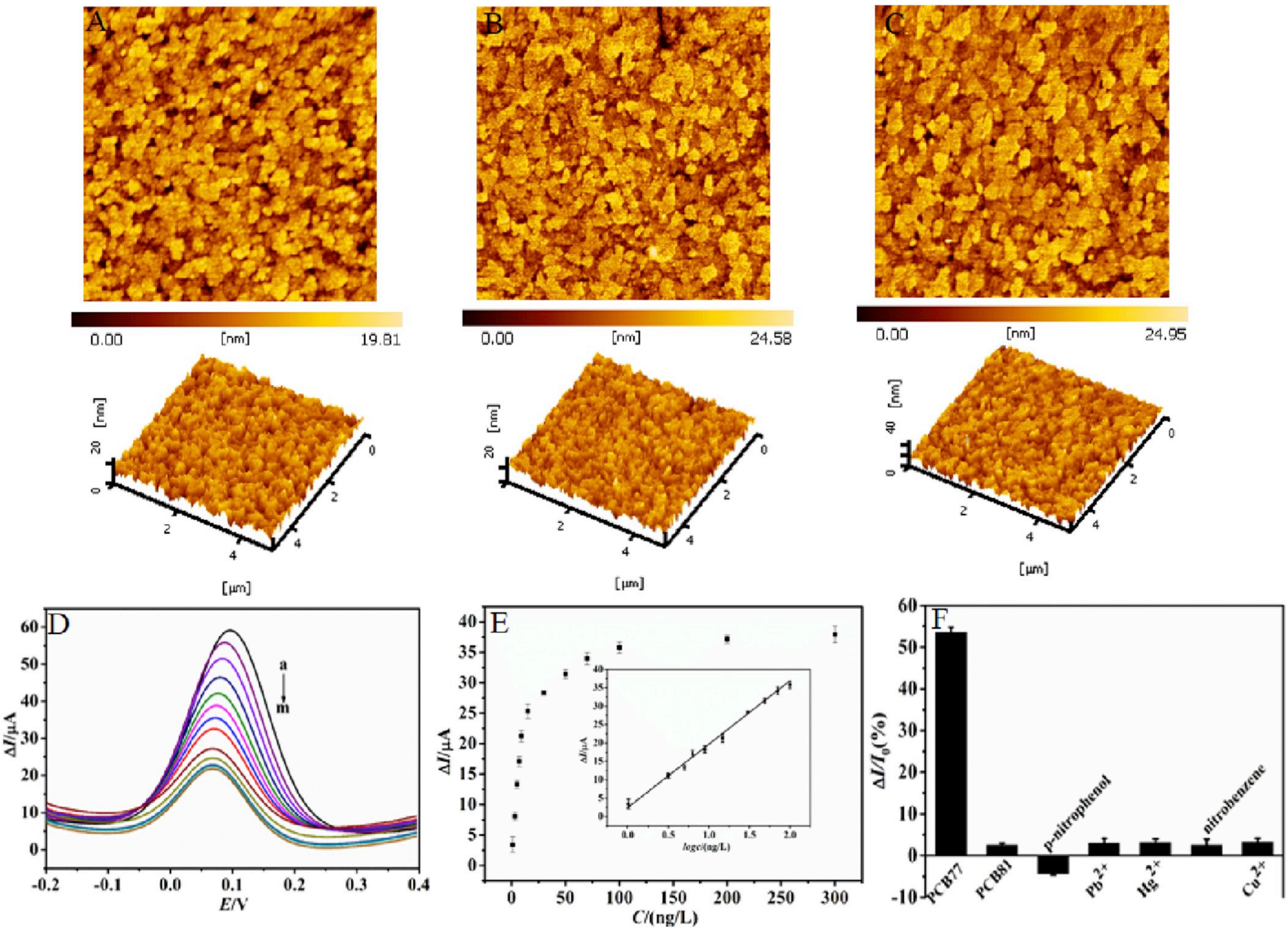

Fig. 4. AFM images (2D and 3D) of NiHCF NPs/rGO hybrids (A), aptamer/NiHCF NPs/rGO (B) and BSA/aptamer/NiHCF NPs/rGO (C) modified electrode; (D) DPV responses of the electrochemical aptasensor in different concentrations of PCB77 (from a to m: 1, 3, 5, 7, 9, 15, 30, 50, 70, 100, 200, 300 ng/L), and (E) Dependence of ΔI on the concentrations of PCB77; Inset: the linear calibration curve of ΔI with logarithm of PCB77 concentrations; (F) The selectivity of the electrochemical aptasensor for PCB77detection.

Table 1
Comparison analytical performances of the present aptasensor with other methods for PCB 77 detection.

Methods	Liner range (ng/L)	Detection limit (ng/L)	Label-free	Stability (storage time)	References
LC-MS	1×10^4–3×10^6	1×10^4	_	_	Portolés et al. (2016)
Colorimetry	1.46×10^2–2.6×10^5	14.6	label-free	_	Cheng et al. (2018)
fluorescence sensor	1×10^2–1×10^5	5×10^2	labeled	_	Xu et al. (2012)
SERS sensor	2.92×10^3–2.92×10^5	9.64×10^3	label-free	84% (one month)	Sun et al. (2016)
Photoelectrochemical biosensor	1×10^4–1×10^6	4.5×10^3	label-free	95.9% (60 min)	Yan et al. (2018)
Electrochemical immunosensor	1×10^4–1×10^6	6×10^3	label-free	_	Centi et al. (2007)
Electrochemical biosensor	2×10^2–2×10^5	10	labeled	86% (10 days)	Wu et al. (2016)
Electrochemical biosensor	1×10^{-1}-1×10^4	0.033	labeled	90% (one week)	Liang et al. (2019)
This work	1–100	0.22	label-free	95.7%(two weeks)	

labeling aptamer or adding electroactive substances to test system to obtain a detectable signal. Besides, some parameters affecting on the sensitivity of the aptasensor were also investigated in order to obtain the optimized analytical performance. First, the analytical performance of the different aptasensors prepared based on different sizes and loading amount of NiHCF NPs on rGO for detecting the same concentration of PCB 77 were investigated by DPV. The size of NiHCF NPs in the hybrids can be tuned by changing the load of NiHCF on the rGO. With increasing the load of NiHCF NPs on rGO, the average diameter from the size of 5 nm increase to 10 nm and 16 nm. The DPV responses of the aptasensors prepared based on different size of NiHCF NPs on rGO were recorded for detecting the same concentration of PCB77. The results indicate that the ΔI value of 12.5 μA for the size of about 5 nm is larger than that of other size. This may be ascribed that more rGO sheets exposure on NiHCF NPs/rGO hybrids with small sizes of NiHCF NPs is more beneficial to the loading of abundant aptamer molecules, especially, can supply larger spaces for aptamer molecules on the interface to make per each binding event effectively. This result confirms further that the combination of the small size of NiHCF NPs and the rGO possess better electrochemical behavior. So the NiHCF NPs/rGO hybrids with average size of about 5 nm NiHCF NPs was used in all of experiments. The reaction time between the aptamer and PCB77 was investigated. The dependence of the peak current change on the reaction time displays in Fig. S8. With the increase of the reaction time, the current change gradually increases.

When the reaction time is 60 min, the current change remains almost constant with increasing the reaction time. So the optimized reaction time is 60 min. Also, the effect of the aptamer modified with different concentrations on the NiHCF NPs/rGO hybrids on PCB 77 detection was also investigated, shown in Fig. S9. The current change increases constantly with increasing of the aptamer concentrations ranging from 0.5 to 2.0 μM. When the concentration of aptamer is over 2.0 μM, the current change reaches the maximum. Thus, 2.0 μM of the aptamer modified concentration on the NiHCF NPs/rGO hybrids is chosen. Meanwhile, the load density of aptamer molecules, Γ_{aptamer}, on the electrode is a key factor affecting the analytical behavior of the aptasensor. Γ_{aptamer}, on the NiHCF NPs/rGO hybrids modified electrode has been estimated to be about 3.83×10^{12} molecules·cm^{-2} by the chronocoulometry using $[\mathrm{Ru(NH_3)_6}]^{3+}$ as a redox label. The detailed calculation is given in Fig. S10. It can be concluded that so large surface density of aptamer on the modified electrode significantly improves the analytical performance of the present aptasensor.

In addition, control experiments were carried out to investigate the selectivity of the electrochemical sensor. Six substances, including PCB81, p-nitrophenol, Pb^{2+}, Hg^{2+}, nitrobenzene and Cu^{2+} were utilized to be as the interferents in control experiments. The aptasensor was immersed in 50.0 ng/L PCB77 or one among six interferents (5 μg/L), respectively. The peak current was recorded for each one and the relative response was calculated from $\Delta I/I_0$ (displayed in Fig. 4F), where ΔI referred to the difference before and after incubation in the different pesticides, respectively, and I_0 referred to the current in the blank solution. The results show that $\Delta I/I_0$ is approximately 53.7% for 50.0 ng/L PCB77, whereas $\Delta I/I_0$ for 100-fold of the interferents is only less than 5.0%, revealing high selectivity of the electrochemical aptasensor for PCB77.

3.4. Stability and reproducibility of electrochemical aptasensor

The aptasensor was immersed in 0.1 M PBS (pH 7.41) at 4 °C for more than two weeks, and then used to determine 50.0 ng/L PCB77. Its stability is investigated by the current change. The result displays that the current change is lower only 3.1% after one week than the initial response and 4.28% after two weeks, indicating the aptasensor has good stability. Six electrochemical aptasensors prepared in the same conditions were used to detect 50.0 ng/L PCB77 to estimate their reproducibility, and the relative standard deviation (RSD) was calculated to be 7.4%. Also, the same aptasensor was used to determine 50.0 ng/L PCB77 for 5 times with the RSD of 5.0%, indicating a good reproducibility of the present aptasensor.

3.5. Application of electrochemical aptasensor

The two real samples, collected from tap water of the laboratory and Lingde lake in the campus of Shanxi University were analyzed by the present aptasensor to evaluate the practical applicability of the electrochemical aptasensor. Before analysis, the lake water sample was centrifuged and filtered using a 0.22 μm membrane, and diluted 100 times with 0.1 M PBS (pH 7.41). Three concentrations of 1.0, 10.0, 100.0 ng/L PCB77 were added to the two water samples, respectively. Meanwhile, all the real samples were analyzed by HPLC to further demonstrate accuracy and reliability of the present aptasensor. The recoveries results in the two samples are displayed in Table S1. It can be observed clearly that the analysis results of the present aptasensor are well consistent with those of HPLC. The average recoveries of the two methods are obtained from 88.0% to 104.1% with the RSD lower than 4.2% (n = 7). The results reveal the aptasensor should be potentially applicable for real environmental sample analysis.

4. Conclusions

In this work, NiHCF NPs/rGO hybrids with small size of about 5 nm NiHCF NPs were synthesized for the first time by in situ co-deposition of NiHCF NPs on rGO. In the hybrids, the rGO supply more space for loading NiHCF NPs and improve the conductivity of the hybrids. The NiHCF NPs acting as a signal probe exhibit a pair of well-defined peaks with highly reversible redox ability and good stability. PCB77 as a model molecule, a simple and label-free electrochemical aptasensor was successfully constructed based on NiHCF NPs/rGO hybrids for detecting PCB77. The prepared electrochemical aptasensor shows high sensitivity and good selectivity for detection of PCB77. Therefore, the established electrochemical sensing platform possesses potential application for on-site detection of PCBs in the environment.

Declaration of competing interest

The authors declare that they have no known competing financial interests or personal relationships that could have appeared to influence the work reported in this paper.

CRediT authorship contribution statement

Lifang Fan: Project administration, Supervision, Resources, Writing - review & editing. **Guizhen Wang:** Data curation, Formal analysis, Writing - original draft. **Wenting Liang:** Software, Visualization. **Wenjun Yan:** Investigation, Methodology. **Yujing Guo:** Supervision, Conceptualization. **Shaomin Shuang:** Supervision. **Chuan Dong:** Supervision. **Yingpu Bi:** Validation, Writing - review & editing.

Acknowledgements

This work was financially supported by the National Natural Science Foundation of China (NSFC, No. 21707082, 21775095 and 21976113), and the Hundred Talent Program of Shanxi Province.

Appendix A. Supplementary data

Supplementary data to this article can be found online at https://doi.org/10.1016/j.bios.2019.111728.

References

Bagkar, N., Betty, C.A., Hassan, P.A., Kahali, K., Bellare, J.R., Yakhmi, J.V., 2006. Thin Solid Films 497, 259–266.

Centi, S., Silva, E., Laschi, S., Palchetti, I., Mascini, M., 2007. Anal. Chim. Acta 594, 9–16.

Chamkasem, N., Lee, S., Harmon, T., 2016. Food Chem. 192, 900–906.

Chen, J., Huang, K.L., Liu, S.Q., Hu, X., 2009. J. Power Sources 186, 565–569.

Chen, T.J., Sheng, A.Z., Hu, Y., Mao, D.S., Ning, L.M., Zhang, J., 2019. Biosens. Bioelectron. 124, 115–121.

Cheng, R.J., Liu, S.Y., Shi, H.J., Zhao, G.H., 2018. J. Hazard Mater. 341, 373–380.

Ciabocco, M., Berrettoni, M., Zamponi, S., Cox, J.A., Marini, S., 2013. J. Solid State Electrochem. 17, 2445–2452.

Fan, L.F., Zhang, C.Y., Yan, W.J., Guo, Y.J., Shuang, S.M., Dong, C., Bi, Y.P., 2019. Talanta 201, pp. 156–164.

Greathead, L., Pantelidis, P., Kelleher, P., Morgan, H., Prodromakis, T., 2016. Biosens. Bioelectron. 86, 805–810.

Habibullah-Al-Mamun, M., Kawser Ahmed, M., Saiful Islam, M., Tokumura, M., Masunaga, S., 2019. J. Ecotox. Environ. Safe. 167, 450–458.

Jeerage, K.M., Steen, W.A., Schwartz, D.T., 2002. Chem. Mater. 14, 530–535.

Jiang, J., Zhang, A.L., Li, L.L., Ai, L.H., 2015. J. Power Sources 278, 445–451.

Kezios, K.L., Liu, X.H., Cirillio, P.M., Kalantzi, O.L., Wang, Y.Z., Petreas, M.X., Park, J.S., Bradwin, G., Cohn, B.A., Factor-Litvak, P., 2012. J. Environ. Health-Glob. 49, 1–11.

Kottegoda, I.R.M., Idris, N.H., Lu, L., Wang, J.Z., Liu, H.K., 2011. Electrochim. Acta 56, 5815–5822.

Kubo, T., Matsumoto, H., Shiraishi, F., Nomachi, M., Nemoto, K., Hosoya, K., Kaya, K., 2007. Anal. Chim. Acta 589, 180–185.

Laviron, E., 1979. J. Electroanal. Chem. 100, 263–270.

Li, N., He, B., Xu, S.Y., Yuna, J.H., Miao, J., Niu, L., Song, J.X., 2012. Mater. Chem. Phys. 133, 726–734.

Li, N., Li, Z.J., Yuan, J.H., Hu, J.G., Miao, J.G., Zhang, Q.X., Niu, L., Song, J.X., 2012. Electrochim. Acta 72, 150–156.

Liang, S., Wu, L.D., Liu, H., Li, J.C., Chen, M.Z., Zhang, M., 2019. Biosens. Bioelectron. 126, 30–35.

Liu, W.L., Zhang, J.F., Li, C., Tang, L., Zhang, Z.Q., Yang, M., 2013. Talanta 104, 204–211.

Lu, Y.L., Huang, Q., Meng, G.W., Wu, L.J., Zhang, J.J., 2014. Analyst 139, 3083–3087.

Magriñá, I., Toldrà, A., Mònica Campàs, M., Ortiza, M., Simonova, A., Katakis, I., Hocek, M., O'Sullivan, C.K., 2019. Biosens. Bioelectron. 124, 115–121.

Ma, X.L., Du, X., Li, X.M., Hao, X.G., Ajay, D., Jagadale, A.D., Abudula, A., Guan, G.Q., 2017. J. Alloy. Comp. 695, 294–301.

Mehta, J., Rouah-Martin, E., Van Dorst, B., Maes, B., Herrebout, W., Scippo, M.L., Dardenne, F., Blust, R., Robbens, J., 2012. Anal. Chem. 84, 1669–1676.

Mkhize, D.S., Nyoni, H., Quinn, L.P., Mamba, B.B., Msagati, T.A.M., 2017. Environ. Sci. Pollut. Res. 12, 11694–11707.

Murati, T., Šimić, B., Pleadin, J., Vukmirovi, M., Mileti, M., Durgo, K., Kniewald, J., Kmetič, I., 2017. Food Chem. Toxicol. 99, 17–23.

Narendra Kumar, A.V., Li, Y.H., Yu, H.J., Yin, S.L., Xue, H.R., Xu, Y., Li, X.N., Wang, H.J., Wang, L., 2018. Electrochim. Acta 292, 107–114.

Peng, X.T., Jiang, L., Gong, Y., Xi-Zhou Hu, X.Z., Peng, L.J., Feng, Y.Q., 2015. Talanta 132, 118–125.

Portolés, T., Sales, C., Abalos, M., Sauló, J., Abad, E., 2016. Anal. Chim. Acta 937, 96–105.

Sassanfar, M., Szostak, J.W., 1993. Nature 364, 550–553.

Sun, K.X., Huang, Q., Meng, G.W., Liu, Y.L., 2016. ACS Appl. Mater. Interfaces 8, 5723–5728.

Sun, S.C., Dou, H.Y., Chuang, M.C., Kolpashchikov, D.M., 2019. Sens. Actuators, B 287, 569–575.

Tuerk, C., Gold, L., 1990. Science 249, 505–510.

Verdian, A., Fooladi, E., Rouhbakhsh, Z., 2019. Talanta 202, 123–135.

Vidimara, V., Licona, C., Cerón-Camacho, R., Guerin, E., Coliat, P., Venkatasamy, A., Ali, M., Guenotg, D., Ronan Le Lagadecd, R.L., Junga, A.C., Freundg, J.N., Pfeffer, M., Mellitzera, G., Savac, G., Gaiddona, C., 2019. Cancer Lett. 440, 145–155.

Wu, L.D., Qi, P.P., Fu, X.C., Liu, H., Li, J.C., Wang, Q., Fan, H., 2016. J. Electroanal. Chem. 771, 45–49.

Wu, T.X., Li, T.T., Liu, Z.G., Guo, Y.J., Dong, C., 2017. Talanta 164, 556–562.

Xu, S.M., Yuan, H., Chen, S.P., Xu, A., Wang, J., Wu, L.J., 2012. Anal. Biochem. 423, 195–201.

Xu, Y.Y., Zhang, M.M., Xiang, J., Deng, C.Y., Wu, H.Y., 2019. Anal. Biochem. 573, 30–36.

Yan, K., Zhu, Y.H., Ji, W.H., Chen, F., Zhang, J.D., 2018. Anal. Chem. 90, 9662–9666.

Yan, Z.D., Gan, N., Wang, D., Cao, Y.T., Chen, M., Li, T.H., Chen, Y.J., 2015. Biosens. Bioelectron. 74, 718–724.

Yang, K.H., Li, Z.Q., Lv, Y.G., Yu, C.Y., Wang, P.L., Su, X.O., Wu, L., He, Y.J., 2018. Anal. Chim. Acta 1041, 94–101.

Yang, Y.Y., Hao, Y.F., Yuan, J.H., Niu, L., Xia, F., 2015. Carbon 84, 174–184.

Youn, D.H., Park, Y.H., Kim, J.Y., Magesh, G., Jang, Y.J., Lee, J.S., 2015. J. Power Sources 294, 437–443.

Zhad, H.R.L.Z., Torres, Y.M.R., Lai, R.Y., 2017. J. Electroanal. Chem. 803, 89–94.

Zhou, Q.H., Wei, T., Liu, Z., Zhang, L.H., Yuan, B., Fan, Z.J., 2019. Electrochim. Acta 303, 40–48.

Zhu, C.H., Meng, G.W., Huang, Q., Huang, Z.L., 2012. J. Hazard Mater. 211, 389–395.